

Signaling gradients in surface dynamics as basis for planarian regeneration

Arnd Scheel · Angela Stevens ·
Christoph Tenbrock

Received: date / Accepted: date

Abstract Based on experimental data, we introduce and analyze a system of reaction-diffusion equations for the regeneration of planarian flatworms. We model dynamics of head and tail cells expressing positional control genes that translate into localized signals which in turn guide stem cell differentiation. Tissue orientation and positional information are encoded in a long range *wnt*-related signaling gradient. Our system correctly reproduces typical cut and graft experiments, and improves on previous models by preserving polarity in regeneration over orders of magnitude in body size during growth phases. Key to polarity preservation in our model flatworm is the sensitivity of cell differentiation to gradients of *wnt*-related signals relative to the tissue surface. This process is particularly relevant in small tissue layers close to cuts during their healing, and modeled in a robust fashion through dynamic boundary conditions.

1 Introduction

Planarians are nonparasitic flatworms commonly found in freshwater streams and ponds [61,63] with a body size in the *mm*-scale. The best experimental data is available for the species "Schmidtea mediterranea", which is 1 *mm* to

A. Scheel

University of Minnesota, School of Mathematics, 206 Church St. S.E., Minneapolis, MN 55455, USA, E-mail: scheel@umn.edu

A. Stevens, Ch. Tenbrock

University of Münster (WWU), Applied Mathematics, Einsteinstr. 62, D-48149 Münster, Germany, E-mail: angela.stevens@wwu.de, christoph.tenbrock@gmail.com

20 *mm* long and consists of 100.000 to more than 2.000.000 cells. Planarians possess the ability to regenerate after rather severe injuries to their body. When small tissue parts are cut from the flatworm - in extreme cases just 0.5% of the original size - these can regenerate to a fully functioning and intact organism [61] with head and tail positioned such that the original orientation of the tissue fragment is respected. When tissue parts are cut from a donor and grafted into a host, the newly created planarian integrates the old positional information of the tissue fragment from the donor with the new positional information it obtains from the host. A better understanding of these processes has a far reaching potential for regeneration in general.

Here, we present a minimal mathematical model, informed by experimental data, that reproduces this fascinating behavior. To the best of our knowledge, our system of reacting and diffusing species is to date the only model that correctly recovers most of the typical cutting and grafting experiments, and preserves polarity during regeneration, even of small tissue fragments. The proposed mechanisms resolve a conundrum in modeling efforts. Many models of spontaneous formation of finite-size structure in unstructured tissue so far, allude to a Turing type mechanism to select a finite wavelength. Activator-inhibitor systems [39], have often been discussed, for instance in the context of regeneration in hydra, which is similarly robust as planarian regeneration. Turing's mechanism however does (intentionally) not scale across several orders of magnitude, nor does it incorporate robust selection of polarity.

1.1 The mathematical model

We focus on the ante-posterior (AP) axis of planarians and consider a one-dimensional domain $x \in [-L, L]$, populated by different cell types and signals. Head cells \mathbf{h} and tail cells \mathbf{d} generate corresponding signals \mathbf{u}_h and \mathbf{u}_d , which activate the respective differentiation of stem cells \mathbf{s} . A long-range *wnt*-related signal \mathbf{w} , in short *wnt*-signal, encodes orientational information through its gradient. It is produced by tail cells in a saturating fashion, and degraded by reactions with head cells:

$$\partial_t s = D_s \partial_{xx} s + \rho_s(s) - p_h u_h s - p_d u_d s, \quad (1.1)$$

$$\partial_t h = D_h \partial_{xx} h + p_h u_h s - \eta_h h, \quad (1.2)$$

$$\partial_t d = D_d \partial_{xx} d + p_d u_d s - \eta_d d, \quad (1.3)$$

$$\partial_t u_h = D_{u_h} \partial_{xx} u_h + h^2(r_0 - r_1 u_h) - r_2 u_h d - r_3 u_h, \quad (1.4)$$

$$\partial_t u_d = D_{u_d} \partial_{xx} u_d + d^2(r_0 - r_1 u_d) - r_2 u_d h - r_3 u_d, \quad (1.5)$$

$$\partial_t w = D_w \partial_{xx} w - p_w h w + p_w d(1 - w). \quad (1.6)$$

Stem cells proliferate with saturating rate and undergo apoptosis [8], which is encoded in $\rho_s(s) = p_s \frac{s}{1+s} - \eta_s s$. Stem cells also differentiate irreversibly into head and tail cells, guided by positional control genes, which are modeled by the respective related localized signals u_h, u_d . Those signals are produced by head and tail cells up to a saturation level, with rates r_0 and r_1 and decay with rate r_3 . This interaction works during both, normal tissue turnover and regeneration [61]. Head and tail cells result from stem cell differentiation and do not proliferate. They undergo apoptosis and degrade the signal associated with the other cell type with rate r_2 .

The quadratic dependence of the production of u_h and u_d on h and d corresponds to higher order molecular kinetics, quadratic here in their simplest form. Replacing these reactions by first-order kinetics, linear in h, d , would result in spontaneous growth of head and tail regions caused by a linear instability of the zero state; see (4.1) in our analysis and model reduction in §4 based on tristability, that is, linear stability of head-only, tail-only, and zero states. The quadratic dependence postulated here suppresses this instability and we suggest that some effective higher-order kinetics are indeed crucial there. We used the same parameter p_w for production and degradation of w , since differing rates showed qualitatively similar outcomes in our simulations. Finally, random motion of cells and diffusion of signal molecules are modeled through the diffusion coefficients D_j .

Writing $U(t, x) = (s, h, d, u_h, u_d, w)(t, x)$, $\mathcal{D} = \text{diag}(D_s, D_h, D_d, D_{u_h}, D_{u_d}, D_w)$ and $\mathcal{F} = (F_s, F_h, F_d, F_{u_h}, F_{u_d}, F_w)$ in the system (1.1)–(1.6), we find

$$\partial_t U = \mathcal{D} U_{xx} + \mathcal{F}(U). \quad (1.7)$$

We prescribe inhomogeneous Dirichlet boundary conditions $U_{x=\pm L} = U_{\pm}$ and evolution equations for the time dependent Dirichlet data

$$\frac{d}{dt} U_{\pm} = -\frac{1}{\gamma} \mathcal{D} \partial_{\nu} U|_{x=\pm L} + \mathcal{F}(U_{\pm}) + \mathcal{B}, \quad (1.8)$$

where $\partial_{\nu} U|_{x=\pm L} = \pm \partial_x U(t, x)|_{x=\pm L}$ denotes the normal derivative. We think of U_{\pm} as concentrations in a boundary compartment of length γ where concentrations are spatially constant. Fluxes $-\frac{1}{\gamma} \mathcal{D} \partial_{\nu} U|_{x=\pm L}$ ensure mass conservation up to kinetics,

$$\begin{aligned} \frac{d}{dt} \left(\int U + \sum_{\pm} \gamma U_{\pm} \right) &= \int \mathcal{F}(U) + \sum_{\pm} \left(\mathcal{D} \partial_{\nu} U|_{\pm L} + \gamma \frac{d}{dt} U_{\pm} \right) \\ &= \int \mathcal{F}(U) + \gamma \sum_{\pm} (\mathcal{F}(U_{\pm}) + \mathcal{B}). \end{aligned}$$

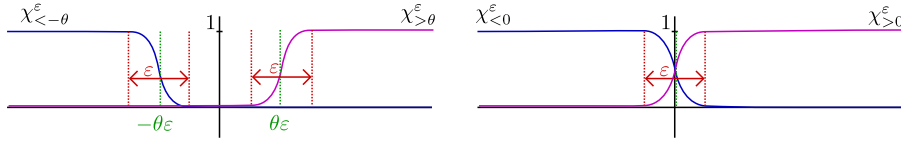


Fig. 1.1: Schematic plot of the smoothed indicator functions χ^ε that detect positive and negative values of the gradient, respectively, with offset θ and sensing thresholds ε .

Kinetics here are identical to those in the bulk of the domain up to a new term \mathcal{B} , present in the dynamics for s_\pm , h_\pm , and d_\pm , that represents a boundary-specific stem-cell differentiation mechanism through rates $\Psi_{h/d}^\pm$,

$$\frac{d}{dt}s_\pm = -\frac{1}{\gamma}D_s \partial_\nu s|_{x=\pm L} + F_s - \Psi_h^\pm s - \Psi_d^\pm s, \quad (1.9)$$

$$\frac{d}{dt}h_\pm = -\frac{1}{\gamma}D_h \partial_\nu h|_{x=\pm L} + F_h + \Psi_h^\pm s, \quad (1.10)$$

$$\frac{d}{dt}d_\pm = -\frac{1}{\gamma}D_d \partial_\nu d|_{x=\pm L} + F_d + \Psi_d^\pm s. \quad (1.11)$$

The differentiation is triggered by lack of head or tail cells, and directed according to the sign of $\partial_\nu w$, explicitly through $\Psi_{h/d}^\pm = \Psi_{h/d}(h, d, \partial_\nu w)|_{x=\pm L}$,

$$\Psi_h = \tau(1-h)(1-d)\chi_{>\theta}^\varepsilon(\partial_\nu w), \quad \text{and} \quad \Psi_d = \tau(1-h)(1-d)\chi_{<-\theta}^\varepsilon(\partial_\nu w).$$

Here $\tau \gg 1$ is the rate of differentiation, and the χ^ε are smoothed versions of the characteristic function, for example

$$\begin{aligned} \chi_{>\theta}^\varepsilon(\xi) &= \frac{1}{2} \left[\tanh((\xi - \varepsilon\theta)/\varepsilon) + 1 \right], \\ \chi_{<-\theta}^\varepsilon(\xi) &= \frac{1}{2} \left[\tanh(-(\xi + \varepsilon\theta)/\varepsilon) + 1 \right]; \end{aligned} \quad (1.12)$$

see Figure 1.1 for an illustration. The steepness ε^{-1} of the smoothed characteristic function can be interpreted as a sensitivity of differentiation with respect to small gradients. The offset θ measures minimal detectable strength of the gradient at the body or wound edge in ε -units. Overall, the kinetics F_s in (1.1) regulate a near-constant supply of stem-cells. As a result, a healthy planarian consists of a high concentration of h near $x = -L$, a high concentration of d near $x = L$, and a near-constant gradient of w in $x \in (-L, L)$; see Figure 1.2.

1.2 Boundary dynamics

Differentiation rates in $\Psi_{h/d}^\pm$ do *not* depend on w itself. In particular, concentration levels of the *wnt*-related (or other long-range) signal w are not

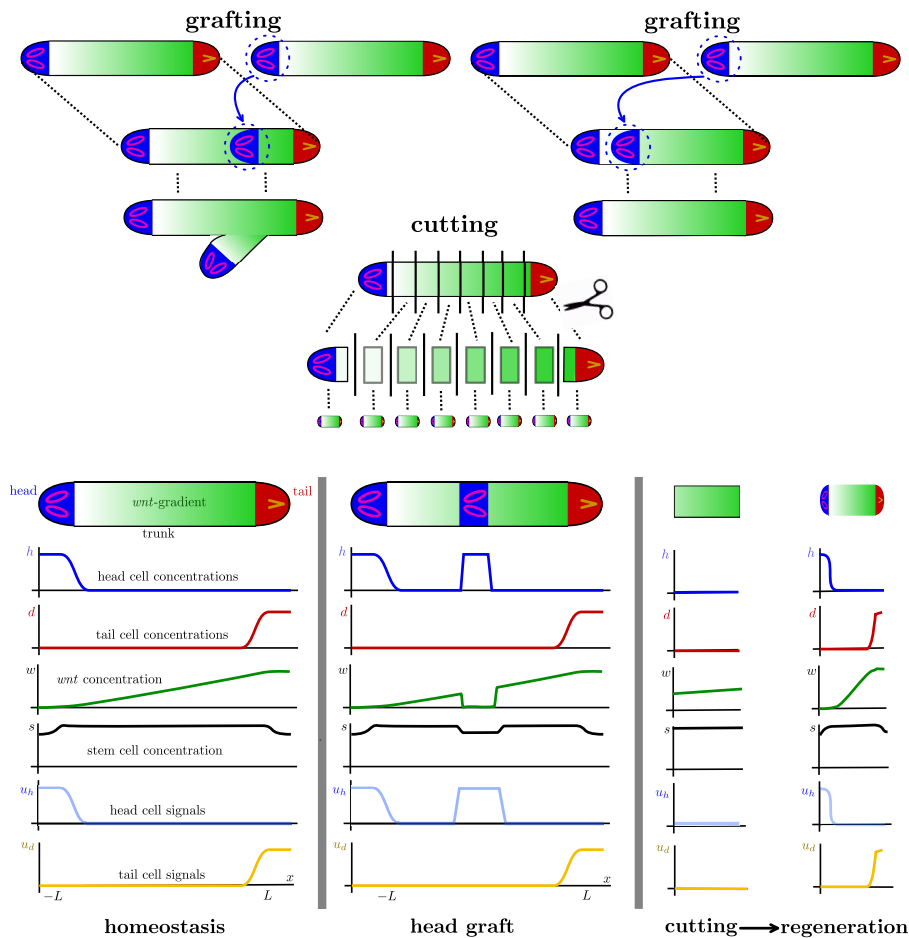


Fig. 1.2: Typical experiments and their representations in terms of our mathematical model. Top left: Schematic illustration of head grafting and regeneration of a two-headed planarian. Top right: Head grafting and regeneration into a normal planarian with one head and tail. Middle row: Cutting experiment and regeneration of eight planarians. Bottom row: Schematic illustration of experiments on planarians and associated spatial distribution of concentrations h , d , w , s , u_h , u_d . Homeostasis (left) has head cells concentrated on the left, tail cells concentrated on the right, a *wnt*-gradient directed towards *wnt*-production in the tail, roughly constant stem cell population with a slight decrease where differentiation into head and tail cells occurs. Head and tail signals are closely mimicking the distribution of head and tail cells. Grafting (center): The head region of a donor is grafted into a host, retaining roughly the distribution of cell concentrations and signaling molecules from its original location. Cutting (right): A thin fragment (here from the trunk region) retains a small *wnt*-gradient but no head or tail cells. Regeneration in this context refers to reestablishing head and tail cell populations while preserving polarity.

converted into positional information that in turn directs the differentiation process. Such a direct conversion of signals is often referred to as a French-flag model (see [86, 87] and, for planarians, [63]) but intentionally not used here:

- 1) Positional information is inherently incapable of explaining preservation of polarity. Since regeneration and polarity are robust with respect to the location of cut out tissue fragments, near head, tail, or from the central body region, absolute levels of w play apparently little role in their regeneration.
- 2) Positional information is not necessary in the early stages of regeneration, but seemingly relevant only later when the size of functional regions like head or tail are regulated; see §6.
- 3) There is little evidence thus far on the nature of robust biological mechanisms that would translate *wnt*-signal levels into differentiation of stem cells. Postulating such mechanisms would simplify the task of reproducing observed phenomena at the (unnecessary) expense of adding a somewhat poorly substantiated regulatory mechanism.

Cutting experiments eliminate head and/or tail cells, thus influence the *wnt*-pathway and destroy the associated signaling gradient. The terms \mathcal{B} in (1.8) model the strong local peak of differentiation of stem cells [82], at wounds inside a formed blastema, guided by *wnt*-signaling [2]. This reaction, which is specific to wounds with loss of tissue, is not completely understood [50], and occurs in our model in regions at the ends of $[-L, L]$. We crucially rely on the detection of the orientation of the *wnt*-gradient relative to the respective body edge. We view this as in some sense necessary, minimal information, to guide regeneration while at the same time preserving polarity. Looking at the boundary after cutting in Figure 1.2, one readily sees that the sign of $\partial_\nu w$ gives clues as to whether differentiation towards head or tail cells should occur.

One can envision several scenarios that enable stem cell differentiation to be guided by gradients of a chemical signal, for instance through comparing signal strength spatially or temporally; see [5], [25]. We do not attempt to model details of this sensing process in the present paper, but simply include a lumped reaction term for differentiation, that depends sharply on the sign of $\partial_\nu w$.

We shall see that our somewhat non standard dynamic (or Wentzel) boundary conditions cannot be readily replaced by, say, Robin boundary conditions. Formally, one could for instance let rates of boundary dynamics tend to infinity or the mass fraction of the boundary compartment γ tend to zero. In the latter case, assuming at the same time rapid reactions \mathcal{N}_1 , in

$$\frac{d}{dt}U_\pm = -\frac{1}{\gamma}\mathcal{D}\partial_\nu U|_{x=\pm L} + \mathcal{N}, \quad \mathcal{N} = \frac{1}{\gamma}\mathcal{N}_1 + \mathcal{N}_2,$$

one finds in the limit the mixed boundary condition $\mathcal{D}\partial_\nu U = \mathcal{N}_1(U)$. In §4.3, we will see that, in this limit to “instantaneous” boundary conditions, the

model does not correctly reproduce the phenomena of regeneration. This mathematical curiosity implies for instance the presence of distinguished body regions relevant in regeneration and may relate to the concept of poles separating head and tail regions from the trunk as discussed in [63] where it is attributed a key role in regeneration.

In another interpretation of dynamic boundary conditions, we can think of compartments for the main body on a uniform grid $x^{(1)}, \dots, x^{(N)}$, with size $x^{(j+1)} - x^{(j)} \equiv dx$ and associated concentrations $U^{(1)}, \dots, U^{(N)}$ such that individual compartments carry masses $dx U^{(j)}$. We now add separate boundary compartments $U^{(0)} = U_-$ and $U^{(N+1)} = U_+$ carrying (larger) masses $\gamma U^{(0)}, \gamma U^{(N+1)}$, independent of dx , and impose no-flux boundary conditions on this inhomogeneous spatial grid. Fixing γ and letting $dx \rightarrow 0$ we arrive at our dynamic boundary condition. Letting $\gamma \rightarrow dx$, we loose the concept of dynamic boundary conditions and should interpret the additional reaction terms \mathcal{B} as nonlinear fluxes. We are not aware of a systematic analysis of such limits, connecting discretization, nonlinear fluxes, and dynamic boundary conditions.

1.3 Outline of the paper

We review biological experiments that motivate our model in §2 and describe numerical simulations that mimic planarian regeneration in various scenarios in §3. In §4, we present analytical results that reduce dynamics to an order parameter c that lumps concentrations of head and tail cells, coupled to the long-range *wnt*-related signal w . This reduction clearly illustrates how the nonlinear boundary fluxes restore head and tail cell concentrations in dependence on the normal derivatives of w , and initiate and organize regeneration. We outline a (in)stability analysis and pinpoint to failure of regeneration, i.e. no recovery of the *wnt*-gradient, when dynamic boundary conditions are relaxed. In a drastic oversimplification, the key feature, namely restoration of a signal gradient through body edge sensing, is distilled in a scalar model for w . Again we outline the limits of regeneration and point to oscillations, caused by coupling of the scalar, non-oscillatory dynamics in the boundary to the diffusive signal field in the bulk and the resulting delayed feedback mechanism. Finally, we remark on other models in the existing literature in §5 and end with a discussion of our results.

2 Planarian regeneration - experiments

Planarians consist of three tissue layers [31], and exhibit a bilateral symmetry, three distinct body axes, a well-differentiated nervous system including a brain, a gastrovascular tract, and a body-wall musculature. Pluripotent adult stem cells (neoblasts), about 30% of the total cell population [7], are the source of all cells [74], and cell types. Neoblasts divide and differentiate constantly. Differentiated cells die after some time. During this dynamic steady state, the flatworm maintains cell type proportions. Planarians and hydra are among the few species that seem to possess a nearly unlimited regenerative ability, recovering from practically every injury, and regenerating when aging. Some asexual planarian species even reproduce by tearing themselves apart and subsequently develop into two intact worms [31]. The ability to replace lost or damaged tissue in humans is very limited. Examples in animals include regeneration of deer antlers, fins of fish, tails of geckos, or complete limbs in some crabs or salamanders. The study of regeneration in biological model organisms holds tremendous appeal and potential for a better understanding of regeneration of human tissue, such as parts of the heart muscle after an infarct.

Cutting. Cutting tissue off a planarian results in regeneration of both parts into an intact organism, more or less independent of position, size, or direction of the cut, with a few exceptions. Each strip of a transverse dissection of the AP-axis will regenerate into a complete flatworm, including an intact brain. In cuts close to head or tail, regeneration of a new head occurs in 3 – 4 weeks. Complete restoration of the right proportions, usually requires 2 – 3 months, [40]. Tissue cut from close to head or tail lacks a pharynx, and draws resources from itself, shrinking to as little as a tenth of its original size, while restoring its basic functions first. Since polarity is preserved, even in small tissue fragments, neighboring cells will regenerate as either head or tail accordingly, after they have been separated by a cut! Exceptions are very long or short fragments, which sometimes regenerate a second head instead of a tail. Too small or too thin cuts are not able to regenerate at all. See Figure 1.2 for the schematics of experiments and the respective representation in our model.

Grafting. Cutting out tissue of an intact donor planarian and transplanting it into another healthy host, the donor usually regenerates as described before, whereas the host may develop new phenotypes; see Figure 1.2. When transplanting parts of the head of the donor into different positions within the host, regeneration depends on the size and position of the donor head tissue within the host. Either a normal flatworm develops, with the grafted second head vanishing, or a second axis is generated at the position of the transplant such that two heads and one tail result, or a two-headed planarian without tail. Outgrowth seems more likely for a larger distance between the head transplant

and the host's head. This is similar for larger head transplants and for tissue taken closer to the donor's head. Transplanting a donor tail into the upper part of a host, sometimes results in a second pharynx in opposite direction, possibly also leading to outgrowth. Transplanting a complete tail fragment below the head fragment of a bisected host, such that just an intermediate strip for a complete planarian is missing, regenerates this missing strip.

Growth and Shrinking. Adult planarians of the species “Schmidtea mediterranea” are roughly 20 mm long if well fed, and can shrink to about 1 mm if starved. When food supply is restored, they regrow while keeping relative proportions and ratios of cell populations intact [7]. For more details on planaria; see [7, 9, 6, 10, 12, 15, 65, 41, 56, 57, 66, 71, 46, 42, 40, 64].

The freshwater polyp hydra, shows a similarly robust regeneration behavior, see [80, 32, 70, 69, 11, 84]. But stem cells in hydra are distributed exclusively inside the body region, below the epithelium. Therefore a tissue fragment consisting only of head or foot cells will not regenerate. See [1] for a quantitative study on induction of additional foot or tail axes. When tissue of hydra is dissociated by pressing it through a net and the resulting fragments are reorganized randomly, a bulb of hydra tissue arises, which subsequently regenerates head and foot structures. Depending on the number of involved cells, several head and body axes occur that will separate only later [47]. Compare Figure 3.5 for a related set-up in our model, which has not yet been described for planarians.

Genetics. Measuring the amount of RNA produced from specific genes during protein synthesis, e.g. through in situ hybridization or northern blot [48], one can identify, which genes are mainly expressed close to head, tail, or after wounding or feeding in planarians. Via RNA interference, short pieces of RNA interact and neutralize targeted mRNA molecules. Thus synthesis of messenger molecules stops at an earlier point in time, and it can be decided, which of the genes being expressed within the head region are actually necessary to regenerate a head. This allows for some analysis of the production dynamics and functioning of related signals (u_h, u_d in our model), even though the corresponding messenger molecules can not be tracked directly so far. Corresponding antibodies are not yet available. We refer to [50], [63] for a review on biological results pertinent to our mathematical model.

Gene expression sites. The three main body axes in planarians are organized by different signaling systems, which seem to act quite independently [60]. This justifies a 1D-model, and we therefore focus on genes which organize the AP-axis. More details can be found in [2, 60, 51, 21, 4, 18, 62].

Among the genes which are expressed close to the head are *notum*, *sFRP-1*, and *sFRP-2*. *Notum* and *sFRP-1* are expressed more locally, while expression of *sFRP-2* extends from the planarian head tip to its center. Genes which

are expressed closer to the tail include *wnt1*, and *wnt11-5* (or *wntP-2*). Here *wnt1* is expressed very locally, while *wnt11-5* is expressed from the tail tip to the center region in a graded fashion. By local expression we mean a few cells producing molecules at the very tips of the planarian, most likely subepidermal muscle cells [85].

The time dynamics of gene expression after wounding are described in [4, 52, 81, 53]; *wnt1*, *wnt11-5*, *notum*, and *sFRP-1* are expressed very early; *wnt1* is expressed first at all wound sites and then normalizes to the behavior described above. Among 128 wound induced genes only *notum* shows a polarized expression [88], i.e. it is expressed at wounds that face missing head structures. Only the cell-internal downstream factor of *wnt*-signaling, β -*catenin* [18], seems to influence this asymmetric expression [67]. Inhibition of *notum* and head amputation prevents head regeneration, while inhibition of *wnt1* and tail amputation prevents tail regeneration. The flatworm will regenerate with two tails or two heads, respectively. Thus *wnt1* and *notum* are expressed very early after wounding and act in an antagonizing manner [26].

The canonical *wnt*-pathway is crucial for establishing and maintaining the polarity along the AP-axis. High levels of *wnt* signaling correlate with high levels of β -*catenin* within the cytoplasm. Inhibiting β -*catenin* leads to different phenotypes [2]. If low doses of inhibitor *dsRNA* are injected into a planarian and the tail is removed, the wound closes but no tail regenerates. Higher doses will lead to regeneration of a second head at the tail wound with a second opposing pharynx in the middle of the planarian body. If the doses are further increased, the pharynx (both) disorganize and ectopic eyes appear. Complete inhibition of β -*catenin* leads to a radially shaped planarian with head-related structures (nerve cells, eyes, etc.) everywhere, even without tail amputation. An organizing β -*catenin* concentration gradient, with maximum at the head and minimum at the tail has been confirmed experimentally [73, 72].

Much of the current understanding of planarian regeneration rests on the idea of a full body gradient of *wnt*-signaling [2], although details are not completely understood. Expression of *wnt1* at tail identities [52] leads to accumulation of β -*catenin* inside the cells [13]. The expression of the *wnt*-antagonist *notum* [26], is exclusively affected by β -*catenin* signaling [67, 53]. It is expressed locally at the tip of the head [60], and required for head regeneration. These mutual dependencies of β -*catenin* and members of the *wnt*-signaling family together with its inhibitors appear to form a *wnt*-related signaling gradient over the planarian body.

In our mathematical model the gradient of w is retained in body fragments, providing clues for polarization in regeneration. We do not take into account

β -catenin or *notum*, since the additional information would be equivalent to $1 - w$ and therefore not contribute in a mathematically essential way.

The hydra homologues of the above mentioned genes *wnt*, *disheveled*, *gsk3*, *tcf* and β -*catenin* seem to act in a comparable way; see [55, 24, 54, 27, 19]. These similarities lead us to suggest that our model for planarians does carry implications also for hydra. The *wnt*-pathway appears to be even more widely conserved during evolution, beyond hydra and planaria.

3 Simulations of cutting, grafting, and growth

Our numerical simulations of system (1.1)-(1.6), (1.9)-(1.11) illustrate homeostasis, cutting, grafting, and growth, confirming and expanding on the schematic representation in Figure 1.2.

Parameter values. Our default parameter values in Table 1 roughly represent expected orders of magnitude within the system. In [75] a non-dimensionalization was performed for a closely related model. Most parameter values do not have a significant effect on the outcome of our simulations and can be changed by several orders of magnitude, with notable exceptions discussed below. Ran-

D_s	1	p_s	200	r_0	18	η_s	100
D_h	10^{-3}	p_h	1	r_1	12	η_h	1
D_d	10^{-3}	p_d	1	r_2	6	η_d	1
D_{u_h}	10^{-2}	p_w	10	r_3	6	τ	0.5
D_{u_d}	10^{-2}	γ	0.3			θ	3
D_w	1	L	10			ε	$2 \cdot 10^{-3}$

Table 1: Parameter values used in simulations throughout, unless noted otherwise. A discussion on the biological measurements and non-dimensionalization can be found in [75].

dom motion of stem cells is of order one as they move fairly freely through the body. Random motion of head and tail cells is very slow. Similarly, the localized signals $u_{h/d}$ diffuse slowly, while the long-range *wnt*-related signal w has a diffusion constant of order 1. We work on domains of length 10 and attribute a mass fraction $\gamma = 0.3$ to the boundary. We assume very fast proliferation of stem cells $p_s \gg 1$ and fast signaling dynamics r_j relative to cell differentiation. Cell differentiation $p_{h/d}$, apoptosis $\eta_{h/d}$, and differentiation at the tissue edges during wound healing τ occur on a time scale of order 1. The production rate of *wnt*-related signals p_w is faster in comparison.

Numerical implementation. We implemented the dynamic boundary conditions as time-dependent Dirichlet conditions. The system was solved with grid

spacing $dx = 0.01$ and time stepping $5 \cdot 10^{-4}$ using a semi-implicit Euler method. We found little changes from refining spatio-temporal grids and also used MATLAB's stiff solver ODE15S for comparison with good agreement.

Results of the numerical simulations. We obtained equilibrium profiles starting with initial conditions that represent head and tail cells in the boundary compartments at the body edges, a uniform distribution of stem cells throughout the trunk, and a uniform *wnt*-signaling gradient. Solving the initial-value problem for a short time, we found that concentrations approached constants in time. Specifically, we used initial conditions

$$\begin{aligned} h_0(x) &\equiv 0, h_{-,0} = 1, h_{+,0} = 0, & d_0(x) &\equiv 0, d_{-,0} = 0, d_{+,0} = 1, & (3.1) \\ s_0(x) &\equiv 1, s_{-,0} = 1, s_{+,0} = 1, & w_0(x) &= \frac{x+L}{2L}, w_{-,0} = 0, w_{+,0} = 1, \end{aligned}$$

and let u_h, u_d equal h, d . The results match the schematics in Figure 1.2. Figure 3.1 illustrates the dynamic stationary profiles of healthy planarians of different body size in our mathematical model. The linear concentration profile

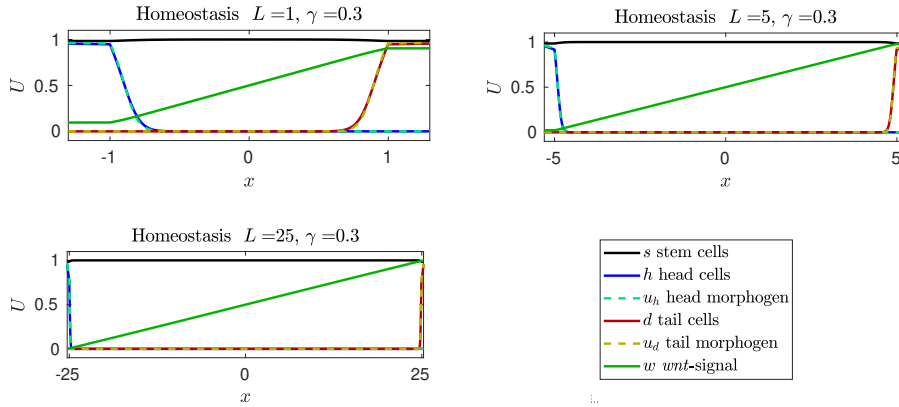


Fig. 3.1: Equilibrium profiles showing a linear *wnt*-signaling profile, head and tail cells concentrated near boundaries, stem cell concentrations with small deviations from constant, and chemical signals closely following head and tail-cell concentrations, respectively. Different scales for x represent different body sizes of planarians. Homeostasis and cutting experiments are illustrated in the supplementary materials CUTTING_SEQUEL.MP4.

in the *wnt*-signal is quite robust under dramatic changes in the domain size. Fixing the width of the boundary compartment γ and varying L we found robust homeostasis between $L = 0.005$ (!) and $L = 40$. For very small L , the total variation of the *wnt*-signal w decreases: w stays bounded away from 0 and 1, and the gradient of w remains bounded for $L \rightarrow 0$. In this regime, the signals u_h and u_d follow the concentrations h and d less closely, being much smaller in amplitude. For very large L , the equilibrium state is sensitive to

small fluctuations since the *wnt*-signaling gradient is small, within $[-\theta \cdot \varepsilon, \theta \cdot \varepsilon]$ where detection of the gradient no longer triggers differentiation. Increasing γ helped stabilize dynamics, and we found robust homeostasis for domain sizes $1, \dots, 50$ and boundary compartments of size $\gamma = 0.1, \dots, 15$. Very small sizes, such as $\gamma = 0.015$, $L = 5$, were not able to sustain a head-trunk-tail profile, consistent with our discussion in §4. Whenever we saw homeostasis, we tested robustness against small amplitude perturbations and found recovery within expected limits, excluding for instance perturbations that alter the sign of the *wnt*-signaling gradient near the boundary.

The localization of the regions occupied by head and tail cells depends first on the strength of random motion D_d, D_h and diffusion rates of their associated morphogens; see Figure 3.2. Changing production and degradation rates r_0, r_1, r_2, r_3 for $u_{h/d}$, one can trigger a spontaneous expansion of the region for head and tail cells, where now the rate of expansion depends on these rates and the diffusivities.

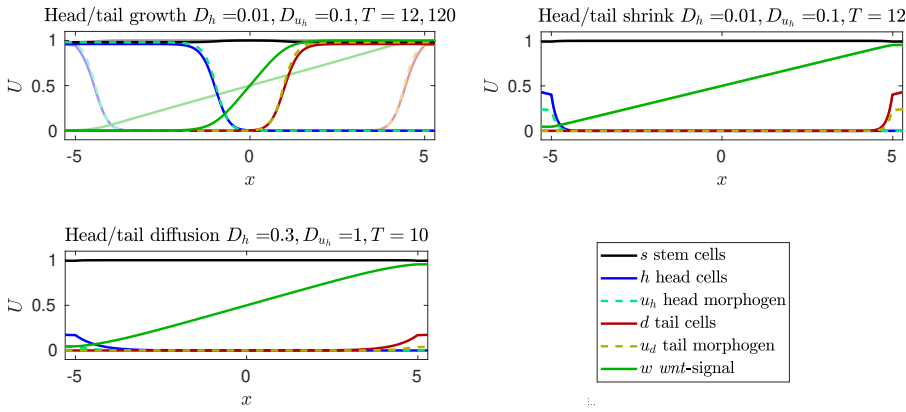


Fig. 3.2: Growing/shrinking of head and tail cell regions (left/right) with $r_0 = 16$, $r_3 = 4$ (top left) and $r_0 = 18$, $r_3 = 10$ (top right); initial conditions as in (3.1). Expansion of head and tail regions (top left) with snapshots at $T = 12$ (translucent) and $T = 120$ (solid); shrinking (top right) terminates at $T = 12$ and homeostasis is reached. Influence of strong random motion and diffusion on homeostasis (bottom left). Other parameters are as in Table 1. See also supplementary material CUTTING_SEQUEL.MP4.

Cutting. Part of the homeostatic state in the central region of the domain is chosen as initial condition

$$w = y_0 + \alpha(x + L)/(2L), \quad s \equiv 1, \quad h \equiv d \equiv u_h \equiv u_d \equiv 0. \quad (3.2)$$

Here, α represents the fraction of the fragment cut, and $y_0 \in [0, 1]$ the concentration of w at the left edge of the cut fragment, corresponding to a cutting

location $x_0 = L(2y_0 - 1) \in [-L, L]$. Thus $\alpha = 0.02$ corresponds to a cut of 2% of body length, and $y_0 = 0.75$ to a cut at three quarters of the body lengths distance from the head. Boundary data is chosen compatible $U_{\pm} = U(\pm L)$ at $t = 0$. Figure 3.3 shows regeneration from cuts of 2% and 4% of body length. Recovery is more sensitive if segments are cut out from tail or head regions. Regeneration depends on the sensitivity ε^{-1} and the threshold θ . Smaller values of ε and θ increase sensitivity and enhance regeneration, but also vulnerability to noise. Smaller mass fractions $\gamma \lesssim 0.03$ in the boundary compartments for $L = 5$ prevent regeneration even for medium-size cuts, to the same extent as homeostasis breaks down. Generally, for cuts near the tail, the head regenerates first, and vice-versa. Polarity is consistently preserved.

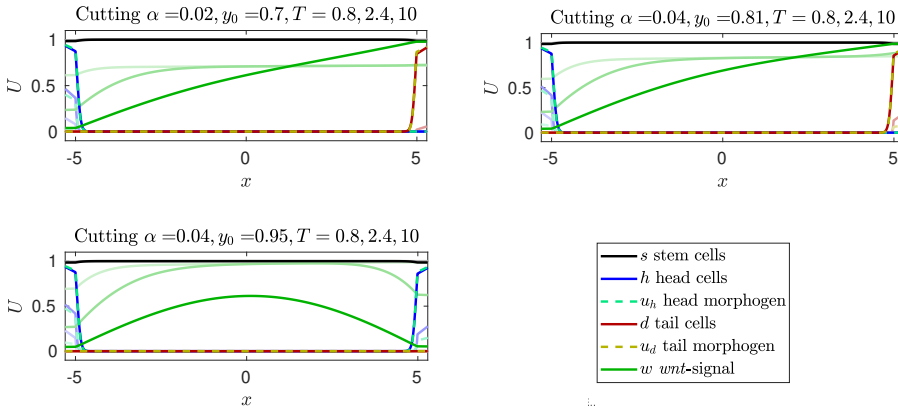


Fig. 3.3: Regeneration after cutting 1/50th from trunk region $y_0 = 0.7$ (top left), 1/25th close to tail $y_0 = 0.815$ (top right) and from tail $y = 0.95$ (bottom left); see (3.2) for initial conditions. Regeneration failure and emergence of heads on both sides, loss of the *wnt*-signaling gradient (bottom left), for a cut very close to the tail region. Parameters are as in Table 1; translucent curves show concentrations at earlier snapshots as listed in the title. Compare video CUTTING_SEQUEL.MP4 in the supplementary materials.

In our numerical simulations, we observed an initial strong burst in differentiation triggered by the boundary sensing $\Psi_{h/d}^{\pm}$. This is compensated for by the strong proliferation of stem cells p_s . Still the stem cell population decreases at the boundary, $s_{\pm} < \frac{1}{2L} \int s$, an effect that is more pronounced for smaller values of p_s or larger τ , thus quantifying the experimentally observed strong proliferation of stem cells during wound healing in our model.

Grafting. Results of homeostasis simulation are used as basis for initial conditions. In a region of a size of 10% of the length of the organism, the concentration of head cells h and u_h is increased to 1, and *wnt*-signaling is eliminated, i.e. $w \equiv 0$, in order to mimic grafting of a head. The head region survives and changes the profile of w . Numerically grafting head cells of a donor close to

the head region of the host leads to merging of the two head regions. Grafting donor head cells near the tail of the host preserves the tail, unless tail cells are significantly destroyed during grafting; see Figure 3.4. The different outcomes reflect the dichotomy seen in experiments where an additional head may grow out of a graft or the graft disappears; see the discussion in §2 and Figure 1.2. We caution here that our simulations rely to some extent on astute choices of production rates for head and tail cells and the associated morphogen, as well as the choice of diffusivity. The boundary between head and trunk cells is nearly stationary and sharply localized. Roughly speaking, an open set of parameter values will lead to expanding head (or tail) regions, a complementary open set will lead to shrinking head (or tail) regions. At the boundary of these parameter regions, head and tail regions will remain nearly stationary, subject only to a slow coarsening interaction as seen in the head-to-head grafting. Stronger diffusivities will enhance both speed of growth and shrinking as well as the slow coarsening. Our parameters are close to the critical values, where head and tail regions neither shrink nor expand. We emphasize that for parameters where head- or tail regions shrink, grafted regions will slowly disappear, but the head- and tail regions near the boundary will persist due to the *wnt*-related gradient triggered differentiation of stem cells. Since regions

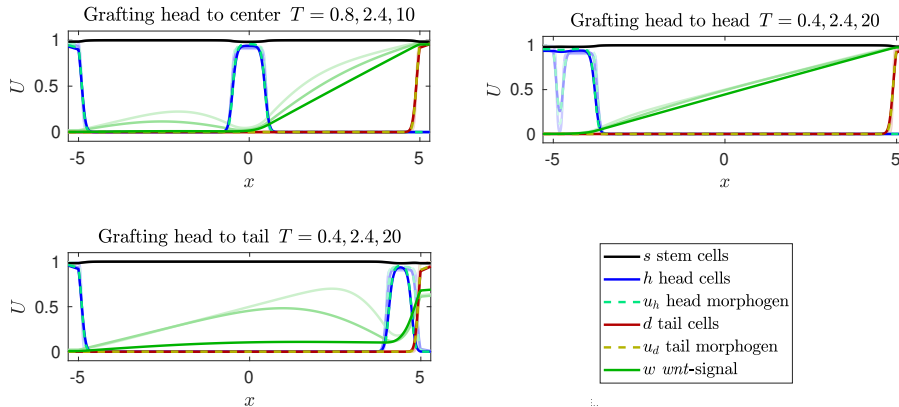


Fig. 3.4: Regeneration after grafting head tissue into center of body (top left), head region (top right), or tail region (bottom left). Parameters are as in Table 1; translucent curves show concentrations at earlier snapshots. Persistence of the grafted head (left panels). Merging (and eventual vanishing) of the graft (top right). Compare also supplement `GRAFTING.MP4`.

between two heads (two tails) do not generate a *wnt*-signaling gradient, our prediction is that secondary cuts from such regions will neither regenerate consistently, nor preserve polarity. These results should be further compared to experiments where possible. Mimicking dissociation experiments in hydra, see

Figure 3.5, we inserted head and tail fragments of roughly 3% of body length randomly at various locations. Larger pieces persist as head and tail regions; smaller pieces eventually disappear.

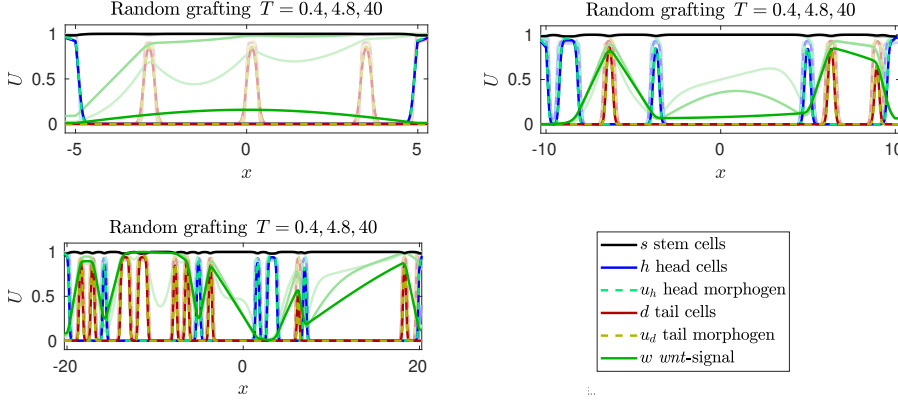


Fig. 3.5: Regeneration after grafting multiple head and tail regions for $L = 10, 20, 40$. Parameters are as in Table 1; translucent curves show concentrations at earlier snapshots. Annihilation of all grafts (top left). Multiple persistent regions for larger domains (top right, bottom left).

Growth. In our simulations for a growing flatworm, the body size expands uniformly at a constant speed $c = 0.3, 1.5, 3$ and we monitor the concentration profiles; see Figure 3.6. More precisely, we assume $x(t) = x(0)(L_0 + ct)/L_0$, where $(-L_0, L_0)$ is the body size at time $t = 0$ and $(-L_0 - ct, L_0 + ct)$ at time t . Mass conservation in the extended domain, in absence of reaction terms, then forces the dilution $\partial_t U(t, x) = \rho(t)U(t, x)$, with $\rho(t) = -c/L(t)$. Transforming back to a fixed domain via the coordinate change $x \mapsto xL_0/L(t)$ gives a diffusion equation on $(-L, L)$ with diffusion matrix $L_0^2 D/L(t)^2$. Therefore in (1.7) we amend the diffusion constant and add a dilution term to model the system on the growing domain,

$$\partial_t U = \mathcal{D}(t)U_{xx} + \mathcal{F}(U) + \rho(t)U, \quad \mathcal{D}(t) = \mathcal{D}L_0^2/L(t)^2, \quad \rho(t) = -c/L(t). \quad (3.3)$$

The relative size of the boundary compartments is preserved, i.e.

$\gamma = \gamma(t) = \gamma(0)L(t)/L_0$, thus introducing the same dilution term in (1.8). Fluxes need to be adjusted to $-\frac{\mathcal{D}(t)}{\gamma(t)}\partial_\nu U$. See [75] for more details on different growth laws and further references.

The resulting system is simulated on a fixed grid corresponding to scaled x -coordinates, but plotted in the actual unscaled x -variables, see Figure 3.6. Parameters are chosen according to Table 1. For slow and moderate growth speeds, the concentration profiles resemble the homeostatic profiles at a given

length. Key features do fail only for rapid expansion. Here $c = 3$ corresponds to a doubling of a flatworm of length 18 in 3 time units, while cell differentiation happens with rate 1, generating at most 1 unit volume of head or tail cells from stem cells in 1 time unit. This failure at rapid growth can be attributed to the dilution of the *wnt*-related signal that is not adequately compensated for by production through tail cells and diffusion, resulting in a very small *wnt*-signaling gradient in the head region. With a gradient close to the sensing limit determined by ε and θ , sensitivity to perturbations increases dramatically.

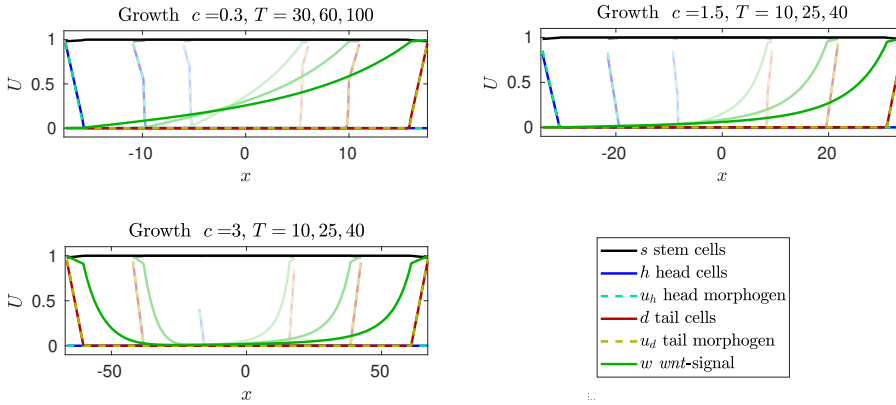


Fig. 3.6: A healthy planarian under uniform linear growth with speeds $c = 0.3, 1.5, 3$. Concentration profiles are plotted in actual coordinates, such that they occupy only part of the final domain at earlier times (faded curves terminate at $\pm(L_0 + cT)$). Profiles are well maintained close to homeostasis for slow (top left) and moderate (top right) growth speeds. For larger speeds (bottom left) dilution of w reduces the overall concentration. The gradient at the left boundary (where $w \sim 0$) falls below the sensing threshold, the concentration of head cells decreases, and a second tail appears.

Our externally imposed growth is clearly not entirely appropriate for actual growth of planarians while feeding. Also, it cannot yet characterize the shrinking dynamics under starvation conditions. The negative dilution term results in an overcrowding of cells with sometimes unstable signaling gradients near the boundary. In an improved model one would like to relate growth laws to proliferation and food supply. Nevertheless, we demonstrated here that our model replicates correctly inherent independence of patterning from body size, and robustness during growth in this simple, first modeling approximation.

4 Analysis via model reduction

Eliminating stem cells and short-range signals. Proliferation of stem cells in (1.1) is much faster than differentiation, $p_s = 200$, $p_h = p_d = 1$. Thus equilibrium concentrations depend only marginally on differentiation, that is, on the concentrations of $u_{h/d}$. Solving for equilibria by setting $\rho_s(s) = 0$, we obtain $s = (p_s - \eta_s)/\eta_s$ which in our choice of parameters gives $s \equiv 1$. Note that our simulations all support this approximation. Having set $s \equiv 1$, we notice that the signal production rates r_j are larger than the cell differentiation and death rates $p_{h/d}$ and $\eta_{h/d}$. Using an adiabatic reduction for the kinetics, one then equilibrates the reaction rates for $u_{h/d}$ and finds $u_{h/d}$ as functions of h and d ,

$$u_h = \frac{r_0 h^2}{r_1 h^2 + r_2 d + r_3}, \quad u_d = \frac{r_0 d^2}{r_1 d^2 + r_2 h + r_3}. \quad (4.1)$$

Similar to the case of stem cell dynamics, the reduction for the kinetics is valid under suitable bounds on gradients, and we shall demonstrate below that such reduced systems capture the key structure of the dynamics quite well. In summary we obtain

$$\begin{aligned} \partial_t h &= D_h \partial_{xx} h + p_h \frac{r_0 h^2}{r_1 h^2 + r_2 d + r_3} - \eta_h h, \\ \partial_t d &= D_d \partial_{xx} d + p_d \frac{r_0 d^2}{r_1 d^2 + r_2 h + r_3} - \eta_d d, \\ \partial_t w &= D_w \partial_{xx} w - p_w h w + p_w d(1 - w), \text{ with boundary data} \\ \frac{d}{dt} h_{\pm} &= -\frac{1}{\gamma} D_h \partial_{\nu} h_{\pm} + p_h \frac{r_0 h_{\pm}^2}{r_1 h_{\pm}^2 + r_2 d_{\pm} + r_3} - \eta_h h_{\pm} + \Psi_h^{\pm}, \\ \frac{d}{dt} d_{\pm} &= -\frac{1}{\gamma} D_d \partial_{\nu} d_{\pm} + p_d \frac{r_0 d_{\pm}^2}{r_1 d_{\pm}^2 + r_2 h_{\pm} + r_3} - \eta_d d_{\pm} + \Psi_d^{\pm}, \\ \frac{d}{dt} w_{\pm} &= -\frac{1}{\gamma} D_w \partial_{\nu} w_{\pm} - p_w h_{\pm} w_{\pm} + p_w d_{\pm} (1 - w_{\pm}), \text{ where again} \\ &\Psi_h(h, d, \partial_{\nu} w) = \tau(1 - h)(1 - d) \chi_{>0}^{\varepsilon}(\partial_{\nu} w), \\ &\Psi_d(h, d, \partial_{\nu} w) = \tau(1 - h)(1 - d) \chi_{<0}^{\varepsilon}(\partial_{\nu} w). \end{aligned} \quad (4.2)$$

Simulations of this reduced model are almost indistinguishable from the full model and therefore not displayed here.

4.1 From cell type to order parameter

In our simulations, concentration profiles of h and d are mostly constant, taking on values $(h_*, 0)$, $(0, d_*)$, or $(0, 0)$, where $h_* = d_* = h_+$,

$$h_{\pm} = \frac{p_h r_0 \pm \sqrt{p_h^2 r_0^2 - 4\eta_h^2 r_1 r_3}}{2\eta_h r_1}, \text{ provided that } p_h^2 r_0^2 > 4\eta_h^2 r_1 r_3,$$

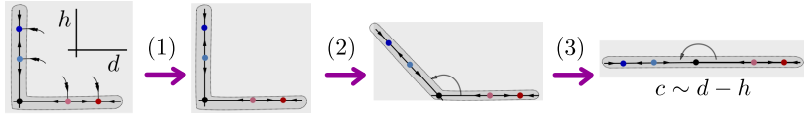


Fig. 4.1: Schematic of the reduction from cell type to order parameter c . In the kinetics of the head-cell dynamics, the ω -limit set of a large ball consists of the line segments of the coordinate axis between the origin and pure-head and pure-tail state, respectively. Restricting to this ω -limit set (1) gives the joined line segments, which one (2) bends open to (3) arrive at a straight one-dimensional line segment with dynamics equivalent to $c \sim d - h$.

which we assume in the sequel. These three states are stable equilibria for the ODE kinetics and the full PDE (4.2) for h, d , when $D_h = D_d$. They correspond to head-only, tail-only, and trunk-only states, respectively. The equilibria $(h_-, 0)$ and $(0, h_-)$ satisfy $0 < h_- < h_+$ and are unstable threshold states, separating initial conditions that evolve toward head cells from initial conditions evolving toward trunk-only cells. The symmetric choice of parameter values, yields equal concentrations of pure head and tail states, but is not necessary to reproduced the phenomena described here.

Regions of constant values of h and d are separated by interfaces (or fronts) that propagate with a speed $= \text{speed}(r_k, \eta_j, p_j)$. The three possible fronts are, head-trunk, tail-trunk, and head-tail. Fronts between pure head and trunk state can be understood in the h -equation, setting $d \equiv 0$.

$$\partial_t h = D_h \partial_{xx} h + g_h(h), \quad g_h(h) = p_h \frac{r_0 h^2}{r_1 h^2 + r_3} - \eta_h h .$$

This equation is a gradient flow related to the free energy $\int D_h \frac{1}{2} h_x^2 + G_h(h)$. Here $G'_h = -g_h$ is the potential with critical points $0, h_{\pm}$. The direction of motion of the front changes sign at the Maxwell point, when $G_h(h_+) = G_h(0)$. For our parameters, fronts propagate slowly toward the head region. Fronts between tail and trunk regions can be described in an equivalent fashion. Fronts between tail and head regions do not propagate due to symmetry if they exist. For our parameter values, such fronts in fact do not appear but front-like initial conditions rather split into two fronts $(h_*, 0) \leftrightarrow (0, 0) \leftrightarrow (0, h_*)$, where the newly emerged state $(0, 0)$ expands. All of those features can be captured in a scalar reaction-diffusion equation. Somewhat formally, on the level of the kinetics, one can envision straightening out the line segments in the $h-d$ -plane $(h_*, 0) \rightarrow (0, 0) \rightarrow (0, d_*)$ into a $1D$ line segment $-1 \rightarrow 0 \rightarrow 1$; see Figure 4.1. In its simplest functional form, tristability is represented by

$$c_t = D_c c_{xx} + c(1 - c^2)(c^2 - \kappa^2), \quad \text{with } 0 < \kappa < 1, \quad (4.3)$$

which possesses stable equilibria $\{-1, 0, 1\}$ corresponding to head-, trunk-, and tail-only states. The odd symmetry $c \rightarrow -c$, mimics the symmetry between d

and h in our simplified model. The critical ‘‘Maxwell’’ point is $\kappa_* = 1/\sqrt{3}$, such that $(0, 0)$ invades $(1, 0)$ and $(0, 1)$ for $\kappa < \kappa_*$ and $(0, 0)$ is invaded otherwise. Similarly to (4.2), fronts between -1 and 1 alias head and tail exist in (4.3) precisely when splitting of the front is not expected, that is, when -1 invades 0 . This can be seen from the phase portrait of the steady-state equation.

Production and degradation now occur for c positive and negative, respectively, reflected in modified w -kinetics

$$w_t = D_w w_{xx} + p_w [c\chi_{>0}^\varepsilon(c)(1-w) + c\chi_{<0}^\varepsilon(c)w]. \quad (4.4)$$

Gradient sensing at the body edges now is lumped together

$$\frac{d}{dt}c_\pm = -\frac{1}{\gamma}D_c\partial_\nu c_\pm + c_\pm(1-c_\pm^2)(c_\pm^2 - \kappa^2) + \Psi_c^\pm, \quad (4.5)$$

$$\frac{d}{dt}w_\pm = -\frac{1}{\gamma}D_w\partial_\nu w_\pm + p_w [c_\pm\chi_{>0}^\varepsilon(c_\pm)(1-w_\pm) + c_\pm\chi_{<0}^\varepsilon(c_\pm)w_\pm], \quad (4.6)$$

$$\text{where } \Psi_c^\pm = \tau\chi_{>\theta}^\varepsilon(-\partial_\nu w|_{\pm L})(1-c_\pm) + \tau\chi_{<-\theta}^\varepsilon(\partial_\nu w|_{\pm L})(-1-c_\pm).$$

System (4.3)–(4.6) forms the minimal model that is able to mimic robust regeneration under cutting, grafting, and growth.

4.2 Homeostasis, cutting, and grafting for system (4.3)–(4.6)

We simulate system (4.3)–(4.6) with parameter values $D_c = 0,001$, $D_w = 1$, $\kappa = 0.577$, $p_w = 10$, $\varepsilon = 0.002$, $\tau = 0.5$, $\theta = 3$, $\gamma = 0.3$, on a domain of size $2L = 10$. Figure 4.2 illustrates prototypical experiments and regeneration with these parameter values. Initial conditions for cutting are

$$w = y_0 + \alpha(x+L)/(2L), \quad c \equiv 0. \quad (4.7)$$

Initial conditions for grafting are $w = 0$ and $c = \pm 1$ on segments of length 1. We chose κ near the Maxwell point, which prevents changes of size in grafting experiments. Different choices of κ lead to expanding or retracting head- or tail regions, similar to the full model as shown in Figure 3.2. Increasing ε or significantly decreasing the mass in the body edge compartments γ prevents recovery. Near critical values of the gradient, the boundary values w_\pm behave non-monotonically; see Figure 4.3. As in the full model, two heads merge for grafts near the host’s head, and one head persists for grafts sufficiently far from the host’s head. This reflects the dichotomy between vanishing of the graft and outgrowth of a new head in experiments.

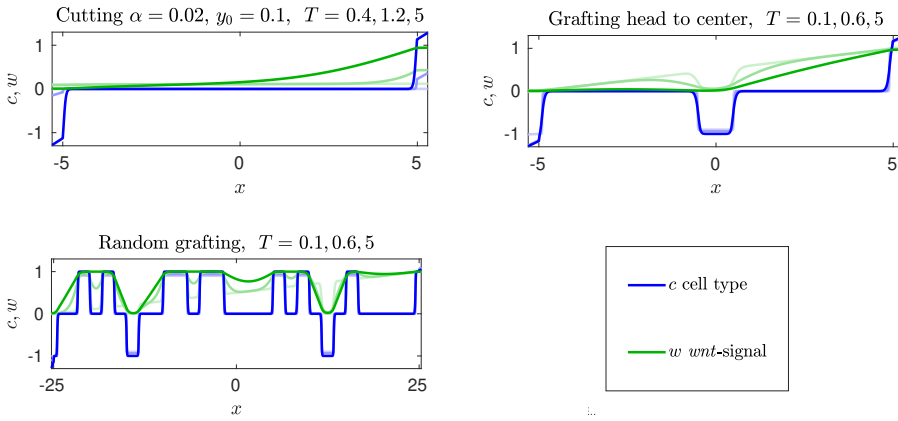


Fig. 4.2: Simulations of the reduced model (4.3)–(4.6) with initial conditions corresponding to cutting (top left), to grafting where a head is grafted into the center (top right), and random grafting of head and tail pieces (bottom left); see text for details.

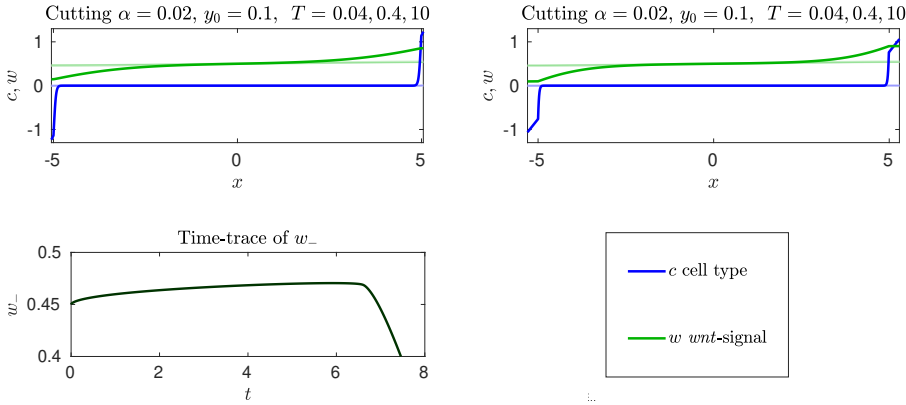


Fig. 4.3: Simulations of the reduced model (4.3)–(4.6) with initial conditions corresponding to cutting, for parameters which cause difficult recovery or recovery failure. Reduction of mass in boundary compartment $\gamma = 0.055$ with $\varepsilon = 0.002$ (top left) leads to slow and non-monotone recovery: the wnt -signaling gradient first decreases before head and tail cell populations are established (top left; associated time series of w_- bottom left). Analogously, larger $\varepsilon = 0.012$ with moderate value $\gamma = 0.3$ slows recovery (top right). Larger ε together with smaller mass fraction prevents recovery.

4.3 Analysis and comparison with Robin boundary conditions.

Throughout this section, let $\theta = 0$. Cutting experiments with small fragments can be thought of as starting with initial conditions close to $c \equiv 0, w \equiv 1/2$, which is a trivial solution of (4.3)–(4.4). Regeneration and its failure can therefore be well predicted from a stability analysis of this solution. Stability would prevent regeneration of small fragments, while instability indicates the onset

of a pattern-forming process. Linearizing at the trivial solution, we find

$$c_t = D_c c_{xx} - \kappa^2 c \quad , \quad w_t = D_w w_{xx} + \frac{1}{2} c \quad , \quad |x| < L$$

$$\frac{d}{dt} c_{\pm} = -\frac{1}{\gamma} D_c \partial_{\nu} c|_{\pm L} - \kappa^2 c_{\pm} + \frac{\tau}{\varepsilon} \partial_{\nu} w|_{\pm L} \quad , \quad \frac{d}{dt} w_{\pm} = -\frac{1}{\gamma} D_w \partial_{\nu} w|_{\pm L} + \frac{1}{2} c_{\pm} .$$

After Laplace transformation, the associated eigenvalue problem can be converted into a transcendental equation which is difficult to analyze. Numerically, one readily finds instabilities in the relevant parameter regimes. We illustrate here the basic instability mechanism with some formal simplifications.

Ignoring the right boundary condition by assuming for instance $x \in (0, \infty)$, eigenfunctions are of the form $c = c_0 e^{-\rho x}$, $w = w_0 e^{-\tilde{\rho} x} + w_1 e^{-\rho x}$, where ρ , $\tilde{\rho}$ are determined by λ , $D_c \rho^2 = \kappa^2 + \lambda$, $D_w \tilde{\rho}^2 = \lambda$, and w_1 depends on c_0 . Substituting into the equations on the boundary at $x = 0$ yields a generalized (since $\rho, \tilde{\rho}$ depend on λ) eigenvalue problem.

$$\lambda c_0 = -\frac{1}{\gamma} D_c (-\rho c_0) - \kappa^2 c_0 + \frac{\tau}{\varepsilon} (\tilde{\rho} w_0 + \rho w_1) \quad , \quad (4.8)$$

$$\lambda w_0 = -\frac{1}{\gamma} D_w (-\tilde{\rho} w_0 - \rho w_1) + \frac{1}{2} c_0 . \quad (4.9)$$

Key are the off-diagonal terms: $\frac{\tau}{\varepsilon} \tilde{\rho} w_0$ from $\frac{\tau}{\varepsilon} \partial_{\nu} w$ in (4.8), and $\frac{1}{2} c_0$ in (4.9). For $\lambda > 0$, these terms are positive hence causing a negative determinant and instability. These off-diagonal terms encode a positive feedback mechanism. A small increase of w_- causes a positive normal derivative for w and hence an increase in c_- at the boundary from the equation for c_- . The increase in c_- translates into a further increase of w_- through $\frac{1}{2} c_-$ in the equation for w_- , thus providing the positive feedback mechanism responsible for instability.

Here the importance of dynamic boundary conditions becomes obvious. Relaxing them by letting reaction rates at the boundary tend to infinity, we formally obtain the mixed Robin boundary conditions: $0 = -\kappa^2 c_{\pm} + \frac{\tau}{\varepsilon} \partial_{\nu} w|_{\pm L}$, $0 = c_{\pm}$. As a consequence, the c -equation decouples as a simple diffusion equation with decay $-\kappa^2 c$ and homogeneous Dirichlet boundary from the dynamic w -boundary condition (!). Setting $c = 0$ then results in a diffusion equation for w with homogeneous Neumann boundary, which implies stability.

This mechanism also elucidates the failure of simpler models with instantaneous adaptation of tail and head cell concentrations, alias order parameter c , to $\text{sign}(\partial_{\nu} w)$ through nonlinear Robin (or mixed) boundary condition $c = \text{sign}(\partial_{\nu} w)$, with a possibly smoothed out sign-function. The idea here is to link c_{\pm} and fluxes $\partial_{\nu} w|_{x=\pm L}$ instantaneously rather than through a time relaxation $\frac{d}{dt} c_{\pm}$ of the boundary data. However, the condition $c = \text{sign}(\partial_{\nu} w)$ will *not* enforce c to increase from 0 to 1, say, in a cutting experiment where $\partial_{\nu} w > 0$.

Instead, the boundary condition is instantaneously satisfied by slightly lowering the concentration of w in a region close to the boundary to achieve $\partial_\nu w = 0$, which is compatible with $c = 0$ at the boundary (with the convention $\text{sign}(0) = 0$). We tested such boundary conditions numerically and observed this predicted decay of the w -gradient near the boundary, and eventual convergence to $c = 0$, that is, failure of regeneration. Relating to the previous discussion, the boundary condition $c = \text{sign}(\partial_\nu w)$ fails to enforce regeneration since it is not explicitly associated with a forced change in levels of c , but acts rather as a nonlinear flux for the w -equation. Dynamic boundary conditions provide precisely this association and therefore guarantee regeneration.

4.4 Recovery of the long-range signal gradient as organizing feature

In our final model simplification, we focus on experiments with only head and tail at the respective extremity, excluding in particular grafting experiments and states with multiple head and tail regions. Assume therefore that the order parameter c mostly vanishes in the domain, that is, head- and tail-cells are confined to the boundary regions. Then the kinetics for w vanish inside the bulk $|x| < L$, and we are left with a simple diffusion equation for w . It is then sufficient to only track boundary values c_\pm of the order parameter. Assuming further that c_\pm adjust rapidly according to (4.5), we can eliminate the order parameter completely setting $c_\pm \sim \text{sign} \partial_\nu w$ and obtain

$$w_t = D_w w_{xx}, \quad |x| < L, \quad \frac{d}{dt} w_\pm = -\frac{1}{\gamma} D_w \partial_\nu w|_{\pm L} + \Psi_w^\pm, \quad (4.10)$$

with $\Psi_w^\pm = \tau [\chi_{<-\theta}^\varepsilon(\partial_\nu w)(-w) + \chi_{>\theta}^\varepsilon(\partial_\nu w)(1-w)]$.

Cutting — numerical experiments. With parameter values $D_w = 1$, $p_w = 10$, $\varepsilon = 0.002$, $\tau = 50$, $\theta = 3$, $\gamma = 0.3$, $L = 10$, Figure 4.4 shows regeneration of small fragments cut from center- or head regions. Recovery is slightly less robust for fragments cut near head or tail. For increasing values of ε , that is, for decreasing sensitivity of gradient sensing at the boundary, we see a transition to a system state which fails to recover; see Figure 4.5. One first observes oscillatory decay toward $w \equiv 0.5$, then sustained oscillations emerge in a weakly subcritical Hopf bifurcation. The unstable periodic orbit separates initial conditions that lead to the trivial, trunk-only state $w \equiv 0.5$ from initial conditions converging to large-scale oscillations. The large oscillations eventually appear to terminate in a heteroclinic bifurcation for larger values of ε . A similar transitions could be observed, for a decreasing mass fraction γ instead of increasing ε .

Analysis — equilibria and stability. For simplicity we assume that $\frac{1}{\gamma} D_w = 1$ and $\theta = 0$ such that the characteristic function takes value $1/2$ at $w = 1/2$.

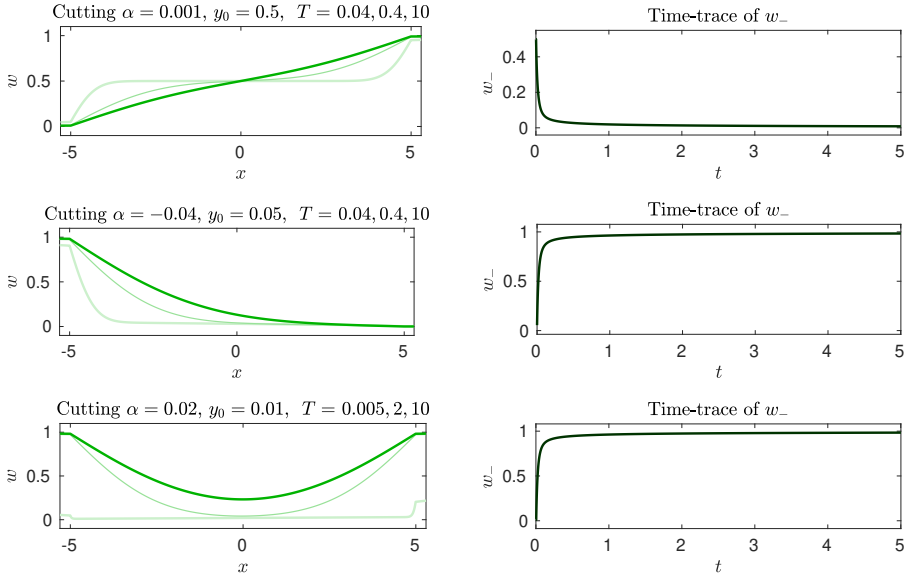


Fig. 4.4: Simulations of (4.10). Initial conditions correspond to cutting experiments, i.e. linear w with small slopes. Top row: robust recovery for a 0.1% fragment from center region. Middle row: recovery for a 4% fragment from head region. This cut is reflected to demonstrate independence of orientation. Bottom row: failure of recovery for a smaller fragment cut from head region. Note the slightly different time instances to see rapid failure of preservation of $\text{sign} \partial_\nu w$ near the boundary. Right column: corresponding time series of w_- .

At the boundary, equilibria then satisfy one of the three conditions,

$$\bullet w = 1, \partial_\nu w > 0; \quad \bullet w = 0, \partial_\nu w < 0; \quad \bullet w = \frac{1}{2}, \partial_\nu w = 0.$$

For moderately sized domains, $1 \ll L \ll \varepsilon^{-1}$, three equilibria result, $w \equiv 1/2$, $w = (x + L)/(2L)$, and $w = (-x + L)/(2L)$, corresponding to only trunk, head-tail, and tail-head solutions. Linearizing at these equilibria, we find

$$w_t = w_{xx}, \quad |x| < L, \quad \frac{d}{dt} w_\pm = -\tau w + \mu \frac{\tau}{\varepsilon} \partial_\nu w, \quad (4.11)$$

where $\mu = 1$ for the trunk solution $w \equiv 0$, and $\mu = 0$ for the head-tail and tail-head solutions. The head-tail and tail-head solutions are always stable. To analyze stability of the trunk-only solution, $\mu = 1$, consider the semi-unbounded domain $x > 0$, set $w = e^{\lambda t + \rho x}$, with $\lambda = \rho^2$, to find the characteristic equation

$$\rho^2 + \frac{\tau}{\varepsilon} \rho + \tau = 0, \quad \rho_\pm = -\frac{\tau}{2\varepsilon} \pm \sqrt{\frac{\tau^2}{4\varepsilon^2} - \tau}, \quad \lambda_\pm = -\frac{\tau}{\varepsilon} \rho_\pm - \tau.$$

For ρ to be an eigenvalue, we need $\text{Re} \rho < 0$. This holds since $\tau, \varepsilon > 0$. We find

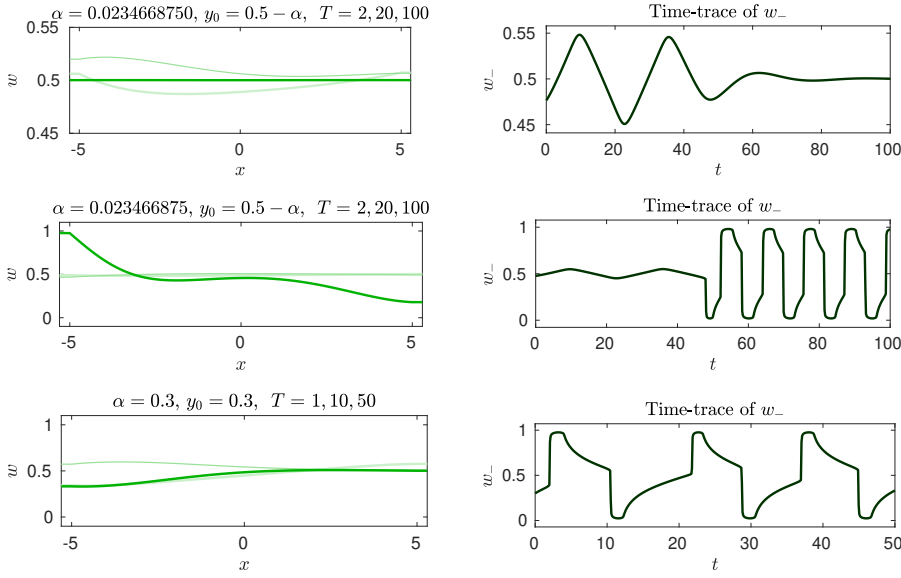


Fig. 4.5: Simulations of (4.10) with initial conditions corresponding to a cutting experiment and sensitivity $\varepsilon^{-1} = 15$. An unstable oscillation separates initial conditions that decay to $w = 0.5$ (top row) from initial conditions with sustained large-amplitude oscillations (middle row) when changing α . Note the different scales for w here. Large stable oscillations disappear in a saddle-node of periodic orbits for smaller ε and in a heteroclinic bifurcation for larger ε , when $\varepsilon^{-1} \sim 12.5$ (bottom row). Also shown are corresponding time series of w_- (right column); see text for predictions of Hopf bifurcations and implications for model corroborations and supplementary materials SCALAR_OSCILLATIONS.MP4 for oscillations.

- *real instability*: $\tau > 4\varepsilon^2$ gives two real roots $\rho_{\pm} < 0$ and two associated real unstable eigenvalues $\lambda_{\pm} > 0$;
- *complex instability*: $2\varepsilon^2 < \tau < 4\varepsilon^2$ gives two complex conjugate roots with $\text{Re}\rho_{\pm} < 0$ and two complex conjugate unstable eigenvalues $\text{Re}\lambda_{\pm} > 0$;
- *Hopf bifurcation*: $2\varepsilon^2 = \tau$ gives two complex conjugate roots with $\text{Re}\rho_{\pm} < 0$ and two purely imaginary eigenvalues $\text{Re}\lambda_{\pm} = 0$, $\text{Im}\lambda_{\pm} = \pm 2i\varepsilon^2$;
- *stability*: $\tau < 2\varepsilon^2$ gives complex conjugate eigenvalues λ_{\pm} with $\text{Re}\lambda_{\pm} < 0$.

Incorporating D_w/γ gives more complicated formulas with similar transitions. The dynamics are quite different if the boundary conditions are relaxed to Robin boundary conditions, for instance

$$\tau [\chi_{<-\theta}^{\varepsilon}(\partial_{\nu}w)(-w) + \chi_{>\theta}^{\varepsilon}(\partial_{\nu}w)(1-w)] = 0, \quad x = \pm L.$$

Again neglecting the flux term $-\frac{1}{\gamma}D_w\partial_{\nu}w$, that is, with sufficiently large mass fractions γ , equilibria for dynamic and Robin boundary conditions coincide. Stability of equilibria is however quite different: the linearization with Robin

boundary conditions is a Sturm-Liouville eigenvalue problem

$$\lambda w = w_{xx}, \quad x \in (-L, L), \quad \frac{\mu}{\varepsilon} \partial_\nu w - w = 0, \quad |x| = L,$$

with real eigenvalues $\lambda_0 > 0 > \lambda_1 > \dots$, $\lambda_0 \sim \varepsilon^2/\mu^2$ for $L \gg 1$. The dynamics generally do not allow for oscillations as observed for periodic boundary conditions. Nevertheless, the trivial trunk-only solution is unstable in this approximation and we see robust recovery of small w -gradients. One can attribute the appearance of oscillations to an effective distributed delay in the otherwise scalar equation for the boundary dynamics of w_- caused by the coupling to the diffusive field $w(t, x)$ which acts as a buffer that stores a blurred history of boundary data.

The transitions discussed here occur when sensitivity w.r.t. the gradient at the boundary is not sufficient, i.e. when ε is too large, or when boundary relaxation τ or the mass fraction γ are too small. This prediction is specific to this model, occurring to some extent also in the full system and the system with order parameter. We are not aware of experimental observations of oscillations in cases where recovery and regeneration are severely impeded. Any such observation would clearly corroborate our basic modeling assumptions.

5 Mathematical models in the literature

Alan Turing, [76] studied the impact of diffusion on pattern formation in reaction-diffusion systems, including also vanishing diffusion. He analyzed the selection of long-, finite-, and short-wavelength patterns, as well as oscillatory, traveling-wave patterns, depending on reaction constants. His key observation was that the spatially extended system can be unstable even when simple kinetics do not exhibit instability, hence the terminology of diffusion-driven instabilities and pattern formation. He also modeled the development of tentacles in hydra [76] but could not finish several follow-up manuscripts on developmental processes in biology [77] due to his untimely death.

Turing's model of two reaction-diffusion equations, especially his 'proof of principle' system, has been tremendously influential, and was used and built upon by others to model, for instance regeneration in hydra, see [20] where the notion of activator-inhibitor system was introduced. For other models based on such kind of dynamics see [44], [45]. The main feature of Turing's mechanism, the selection of a preferred finite wavelength for a fixed domain size, like for the tentacles of hydra, turns into a drawback for the regeneration of hydra's or the planarian body axis. The patterns developing during its regeneration are robust over several orders of magnitudes in body size. Attempts to address this conundrum typically built on additional species that evolve dynamically and

affect reaction constants in Turing's mechanism in ways that change selected wavelengths. In well designed contexts scaling invariance of patterns can be covered for large changes in domain size [49,79,78,83]. For such models on scale-independent patterning in zebra fish see [3].

In planarians, regeneration necessitates establishing a monotone signaling gradient. Generation of such monotone structures has been studied mathematically quite extensively in the context of phase separation [17] and cell polarization [43]. In the reaction-diffusion context, the simplest formulations lead to 2-species mass-conserving systems, which can exhibit patterns, albeit with a wavelength proportional to the domain. Patterns of smaller wavelength are unstable against coarsening although coarsening can be slow or even arrested for small or vanishing diffusivities.

Motivated by a receptor-ligand binding system [68], regeneration of hydra was modeled in [33] via diffusion driven instabilities. Introduction of hysteresis allowed to correctly recover grafting experiments in simulations of six coupled ODEs and PDEs [34]. Intuitively, hysteresis or multistability are well suited to describe the outcome of grafting experiments, as higher values of variables for head identities, are stabilized, independent of position or domain size. The absorption of very small transplants might also be explainable. In fact, our model contains some features of the associated multistability. The above models though do typically not generate patterns corresponding to cutting and dissociation experiments robustly. Systems of ODEs (vanishing diffusivities) coupled to PDEs have been studied more recently w.r.t. their pattern-forming capabilities [36,35,22,37,30,38], like stable patterns and unbounded solutions developing spikes. The role of hysteresis in diffusion-driven instabilities and de novo formation of stable patterns was investigated in [23,29].

The emphasis on separating boundary and bulk dynamics in our approach relates to recent efforts in understanding the the role surface reactions and bulk-to-surface coupling in morphogenesis [16,14,28,58,59]. In such a setup, species that react and diffuse with similar diffusion constants on a surface would not form patterns. If, however, one of the species diffuses rapidly into, within, and back from the bulk, an effective large diffusivity for this species ensues, which in turn enables a diffusion driven instability towards stable patterns; see for instance [75] for a more in-depth discussion and a model related to ours, but differing w.r.t. the boundary dynamics and gradient sensing.

We emphasize however that our model is very different in essential features from models in the literature described here, arguably simpler, at least in the reduced forms of §4, and possibly more versatile in regard to the experimental phenomenology that can be robustly reproduced.

6 Discussion

We presented a mathematical model for robust regeneration of planarians which reproduces most cutting and grafting experiments. Our system preserves polarity after cutting and yields robust results over organism scales differing by factors of 100. Central are two strong indications from experiments:

- (i) sharply increased activity including stem cell proliferation near wounds;
- (ii) global gradients of chemical signals, related to the *wnt*-signaling pathway.

The first observation is translated into dynamic boundary condition, modeling changed reaction kinetics in a boundary compartment at the body edges. The second observation has often been discussed in connection with the regulation of tissue size, expanding on the idea of the French-flag model. In contrast to this, we postulate that the gradient itself, rather than absolute levels of the signal are relevant for the stem cell population and, at wound sites, is translated into directed differentiation. We suspect that within a rather general modeling context, effective gradient sensing is necessary in order to reproduce robust preservation of polarity in cutting experiments, suggesting that such processes may indeed be relevant also in real planarians.

We incorporate these ingredients into a comprehensive model of 3 cell type populations and 3 chemical signals. Through model reduction to one order parameter for cell types and one long-range chemical signal, only, we exhibit how the regeneration process is organized. One can point to regeneration as an instability mechanism for a trivial, unpatterned state and identify analytically limits of robust regeneration. The process is fundamentally different from Turing type mechanism, and driven by boundary dynamics.

Outlook. There are several ways in which our model could be refined. First, a head over tail bias, which is observed in experiments, could be introduced for instance through different sensing thresholds θ at body edges, or different differentiation and proliferation kinetics. We are, however, not aware of a causal rather than a phenomenological justification of this bias. Second, we did not attempt to model regulation of the size of the head and tail regions. Our model relies essentially on establishing a global signaling gradient. Thus cells could in principle obtain positional information by reading out absolute levels of the *wnt*-related signal. Postulating such a w -dependence for differentiation or apoptosis in the $\{s, h, d, u_h, u_d\}$ -subsystem, one could influence the tristability. Front motion as described in §4.1 would then depend on w levels, and stationary interfaces would lock into fixed w -levels, thus regulating a fixed size of head or tail as a percentage of the full body length. In the order parameter model, this could for instance be accomplished by

$$c_t = c_{xx} + c(1 - c^2)(c - \chi_{>0.85}^\varepsilon(w)) (c - \chi_{<-0.85}^\varepsilon(w)) ,$$

which would regulate the size of head and tail to regions where $w > 0.85$ and $w < -0.85$, respectively, about 15% of body size, each. Such effects could also model the spontaneous formation of head cell clusters when suppressing the *wnt*-signaling pathway. Lastly, one could address directed motion of stem cells or progenitors. Migratory stages of progenitors from their place of birth to their site of terminal differentiation are discussed in [63]. Taking such effects into account could potentially improve further, both qualitatively and quantitatively on the results presented here.

Acknowledgments. CT was supported by a fellowship of the Graduate School of the Cells-in-Motion Cluster of Excellence EXC 1003-CiM, University of Münster (WWU). ASc was partially supported through NSF grants DMS-1311740 and DMS-1907391, a Research Award from the Alexander-von-Humboldt Foundation, and a WWU Fellowship. ASc and ASt were supported by the DFG (German Research Foundation) under Germany's Excellence Strategy EXC 2044-390685587, Mathematics Münster: Dynamics – Geometry – Structure. CT and ASt gratefully acknowledge numerous valuable discussions about the biology of planarians with Kerstin Bartscherer.

References

1. J. Achermann and T. Sugiyama. Genetic analysis of developmental mechanisms in hydra: X. Morphogenetic potentials of a regeneration-deficient strain (reg-16). *Developmental biology*, 107(1):13–27, 1985.
2. T. Adell, F. Cebrià, and E. Saló. Gradients in planarian regeneration and homeostasis. *Cold Spring Harbor perspectives in biology*, 2(1):a000505, 2010.
3. M. Almuedo-Castillo, A. Bläßle, D. Mörsdorf, L. Marcon, G. H. Soh, K. W. Rogers, A. F. Schier, and P. Müller. Scale-invariant patterning by size-dependent inhibition of nodal signalling. *Nature Cell Biology*, 20(9):1032–1042, 2018.
4. M. Almuedo-Castillo, M. Sureda-Gómez, and T. Adell. Wnt signaling in planarians: new answers to old questions. *Internat. J. of Develop. Biol.*, 56(1-2-3):53–65, 2012.
5. W. Alt. Biased random walk models for chemotaxis and related diffusion approximations. *Journal of Mathematical Biology*, 9(2):147–177, 1980.
6. J. Baguña. Mitosis in the intact and regenerating planarian *Dugesia mediterranea* n. sp. II. Mitotic studies during regeneration, and a possible mechanism of blastema formation. *Journal of Experimental Zoology*, 195(1):65–79, 1976.
7. J. Baguña and R. Romero. Quantitative analysis of cell types during growth, degrowth and regeneration in the planarians *Dugesia mediterranea* and *Dugesia tigrina*. In *The Biology of the Turbellaria*, pages 181–194. Springer, 1981.
8. J. Baguña, R. Romero, E. Saló, J. Collet, C. Auladell, M. Ribas, M. Riutort, J. García-Fernández, F. Burgaya, and D. Bueno. Growth, degrowth and regeneration as developmental phenomena in adult freshwater planarians. In *Experimental embryology in aquatic plants and animals*, pages 129–162. Springer, 1990.
9. J. Baguña, S. Carranza, M. Pala, C. Ribera, G. Giribet, M. A. Arnedo, M. Ribas, and M. Riutort. From morphology and karyology to molecules. new methods for taxonomical identification of asexual populations of freshwater planarians. a tribute to professor mario benazzi. *Italian Journal of Zoology*, 66(3):207–214, 1999.

10. C. R. Bardeen and F. Baetjer. The inhibitive action of the roentgen rays on regeneration in planarians. *Journal of Experimental Zoology Part A: Ecological Genetics and Physiology*, 1(1):191–195, 1904.
11. H. R. Bode. Head regeneration in Hydra. *Develop. Dyn.*, 226(2):225–236, 2003.
12. I. Bowen, T. Ryder, and J. Thompson. The fine structure of the planarian *Polycelis tenuis* Iijima. *Protoplasma*, 79(1-2):1–17, 1974.
13. C. Cramer von Laue. *Untersuchungen zur dualen Funktion von β -Catenin im Wnt-Signalweg und der Cadherin-vermittelten Zelladhäsion bei Hydra*. PhD thesis, Technische Universität Darmstadt, 2003.
14. D. Cusceddu, L. Edelstein-Keshet, J. Mackenzie, S. Portet, and A. Madzvamuse. A coupled bulk-surface model for cell polarisation. *Journal of Theoretical Biology*, 2018.
15. E. De Vries, J. Baguña, and I. Ball. Chromosomal polymorphism in planarians (Turbellaria, Tricladida) and the plate tectonics of the western Mediterranean. *Genetica*, 62(3):187–191, 1984.
16. C. M. Elliott, T. Ranner, and C. Venkataraman. Coupled bulk-surface free boundary problems arising from a mathematical model of receptor-ligand dynamics. *SIAM J. Math. Anal.*, 49(1):360–397, 2017.
17. P. C. Fife. Models for phase separation and their mathematics. *Electron. J. Differential Equations*, pages No. 48, 26, 2000.
18. M. Gagliardi, A. Hernandez, I. J. McGough, and J.-P. Vincent. Inhibitors of endocytosis prevent Wnt/Wingless signalling by reducing the level of basal β -catenin/Armadillo. *J Cell Sci*, 127(22):4918–4926, 2014.
19. L. Gee, J. Hartig, L. Law, J. Wittlieb, K. Khalturin, T. C. Bosch, and H. R. Bode. β -catenin plays a central role in setting up the head organizer in hydra. *Developmental biology*, 340(1):116–124, 2010.
20. A. Gierer and H. Meinhardt. A theory of biological pattern formation. *Kybernetik*, 12(1):30–39, 1972.
21. K. A. Gurley, S. A. Elliott, O. Simakov, H. A. Schmidt, T. W. Holstein, and A. S. Alvarado. Expression of secreted Wnt pathway components reveals unexpected complexity of the planarian amputation response. *Developmental biology*, 347(1):24–39, 2010.
22. S. Härting and A. Marciniak-Czochra. Spike patterns in a reaction–diffusion ode model with Turing instability. *Math. Meth. in the Applied Sciences*, 37(9):1377–1391, 2014.
23. S. Härting, A. Marciniak-Czochra, and I. Takagi. Stable patterns with jump discontinuity in systems with Turing instability and hysteresis. *Disc. Cont. Dyn. Sys. A.*, 38:757–800, 2017.
24. B. Hobmayer, F. Rentzsch, K. Kuhn, C. M. Happel, C. C. von Laue, P. Snyder, U. Rothbächer, and T. W. Holstein. WNT signalling molecules act in axis formation in the diploblastic metazoan Hydra. *Nature*, 407(6801):186–189, 2000.
25. M. Iijima, Y. E. Huang, and P. Devreotes. Temporal and Spatial Regulation of Chemotaxis. *Developmental Cell*, 3:469–478, 2002.
26. S. Kakugawa, P. F. Langton, M. Zebisch, S. A. Howell, T.-H. Chang, Y. Liu, T. Feizi, G. Bineva, N. O’Reilly, A. P. Snijders, et al. Notum deacylates Wnt proteins to suppress signalling activity. *Nature*, 519(7542):187–192, 2015.
27. T. Lengfeld, H. Watanabe, O. Simakov, D. Lindgens, L. Gee, L. Law, H. A. Schmidt, S. Özbek, H. Bode, and T. W. Holstein. Multiple Wnts are involved in Hydra organizer formation and regeneration. *Developmental biology*, 330(1):186–199, 2009.
28. H. Levine and W.-J. Rappel. Membrane-bound Turing patterns. *Phys. Rev. E (3)*, 72(6):061912, 5, 2005.
29. Y. Li, A. Marciniak-Czochra, I. Takagi, and B. Wu. Steady states of fitzhugh-nagumo system with non-diffusive activator and diffusive inhibitor. *preprint*, 2017.
30. Y. Li, A. Marciniak-Czochra, I. Takagi, B. Wu, et al. Bifurcation analysis of a diffusion-ode model with Turing instability and hysteresis. *Hiroshima Mathematical Journal*, 47(2):217–247, 2017.

31. D. Lobo, W. S. Beane, and M. Levin. Modeling planarian regeneration: a primer for reverse-engineering the worm. *PLoS Comput Biol*, 8(4):e1002481, 2012.
32. H. K. MacWilliams. Hydra transplantation phenomena and the mechanism of hydra head regeneration: II. Properties of the head activation. *Developmental biology*, 96(1):239–257, 1983.
33. A. Marciniak-Czochra. Receptor-based models with diffusion-driven instability for pattern formation in hydra. *Journal of Biological Systems*, 11(03):293–324, 2003.
34. A. Marciniak-Czochra. Receptor-based models with hysteresis for pattern formation in hydra. *Mathematical biosciences*, 199(1):97–119, 2006.
35. A. Marciniak-Czochra, S. Härtling, G. Karch, and K. Suzuki. Dynamical spike solutions in a nonlocal model of pattern formation. *Nonlinearity*, 31(5):1757–1781, 2018.
36. A. Marciniak-Czochra, G. Karch, and K. Suzuki. Instability of Turing patterns in reaction-diffusion-ode systems. *Journal of Mathematical Biology*, 74(3):583–618, 2017.
37. A. Marciniak-Czochra, G. Karch, K. Suzuki, J. Zienkiewicz, et al. Diffusion-driven blowup of nonnegative solutions to reaction-diffusion-ode systems. *Differential and Integral Equations*, 29(7/8):715–730, 2016.
38. A. Marciniak-Czochra, M. Nakayama, I. Takagi, et al. Pattern formation in a diffusion-ode model with hysteresis. *Differential and Integral Equations*, 28(7/8):655–694, 2015.
39. H. Meinhardt. Turing’s theory of morphogenesis of 1952 and the subsequent discovery of the crucial role of local self-enhancement and long-range inhibition. *Interface Focus*, 2(4):407–416, 2012.
40. T. H. Morgan. Experimental studies of the regeneration of *Planaria maculata*. *Development Genes and Evolution*, 7(2):364–397, 1898.
41. T. H. Morgan. The control of heteromorphosis in *Planaria maculata*. *Archiv für Entwicklungsmechanik der Organismen*, 17(4):683–695, 1904.
42. T. H. Morgan. Polarity considered as a phenomenon of gradation of materials. *Journal of Experimental Zoology*, 2(4):495–506, 1905.
43. Y. Mori, A. Jilkine, and L. Edelstein-Keshet. Wave-pinning and cell polarity from a bistable reaction-diffusion system. *Biophysical journal*, 94(9):3684–3697, 2008.
44. J. D. Murray. *Mathematical biology I: An introduction*. Interdisciplinary Applied Mathematics, 17. Springer-Verlag, New York, 2002.
45. J. D. Murray. *Mathematical biology II: Spatial models and biomedical applications*. Interdisciplinary Applied Mathematics, 18. Springer-Verlag, New York, 2003.
46. P. A. Newmark and A. S. Alvarado. Not your father’s planarian: a classic model enters the era of functional genomics. *Nature Reviews Genetics*, 3(3):210–219, 2002.
47. K. Noda. Reconstitution of dissociated cells of hydra. *Zool. Mag.*, 80:99–101, 1971.
48. C. Nüsslein-Volhard and E. Wieschaus. Mutations affecting segment number and polarity in *Drosophila*. *Nature*, 287(5785):795–801, 1980.
49. H. G. Othmer and E. Pate. Scale-invariance in reaction-diffusion models of spatial pattern formation. *Proc. of the National Academy of Sciences*, 77(7):4180–4184, 1980.
50. S. Owlarn and K. Bartscherer. Go ahead, grow a head! A planarian’s guide to anterior regeneration. *Regeneration*, 3(3):139–155, 2016.
51. C. P. Petersen and P. W. Reddien. Smed- β catenin-1 is required for anteroposterior blastema polarity in planarian regeneration. *Science*, 319(5861):327–330, 2008.
52. C. P. Petersen and P. W. Reddien. A wound-induced Wnt expression program controls planarian regeneration polarity. *Proceedings of the National Academy of Sciences*, 106(40):17061–17066, 2009.
53. C. P. Petersen and P. W. Reddien. Polarized notum activation at wounds inhibits Wnt function to promote planarian head regeneration. *Science*, 332(6031):852–855, 2011.
54. I. Philipp, R. Aufschnaiter, S. Özbek, S. Pontasch, M. Jenewein, H. Watanabe, F. Rentzsch, T. W. Holstein, and B. Hobmayer. Wnt/ β -catenin and noncanonical Wnt signaling interact in tissue evagination in the simple eumetazoan Hydra. *Proceedings of the National Academy of Sciences*, 106(11):4290–4295, 2009.

55. G. Plickert, V. Jacoby, U. Frank, W. A. Müller, and O. Mokady. Wnt signaling in hydroid development: the primary body axis in embryogenesis and its subsequent patterning. *Developmental biology*, 298(2):368–378, 2006.
56. H. Randolph. The regeneration of the tail in Lumbriculus. *Journal of Morphology*, 7(3):317–344, 1892.
57. H. Randolph. Observations and experiments on regeneration in planarians. *Development Genes and Evolution*, 5(2):352–372, 1897.
58. A. Rätz and M. Röger. Turing instabilities in a mathematical model for signaling networks. *J. Math. Biol.*, 65(6-7):1215–1244, 2012.
59. A. Rätz and M. Röger. Symmetry breaking in a bulk-surface reaction-diffusion model for signalling networks. *Nonlinearity*, 27(8):1805–1827, 2014.
60. P. W. Reddien. Constitutive gene expression and the specification of tissue identity in adult planarian biology. *Trends in Genetics*, 27(7):277–285, 2011.
61. P. W. Reddien and A. S. Alvarado. Fundamentals of planarian regeneration. *Annu. Rev. Cell Dev. Biol.*, 20:725–757, 2004.
62. H. Reuter, M. März, M. C. Vogg, D. Eccles, L. Grífol-Boldú, D. Wehner, S. Owlarn, T. Adell, G. Weidinger, and K. Bartscherer. β -catenin-dependent control of positional information along the AP body axis in planarians involves a teashirt family member. *Cell Reports*, 10(2):253–265, 2015.
63. J. C. Rink. *Stem Cells, Patterning and Regeneration in Planarians: Self-Organization at the Organismal Scale*, pages 57–172. Springer, New York, 2018.
64. E. Saló and J. Baguña. Regeneration and pattern formation in planarians. *Development*, 83(1):63–80, 1984.
65. E. Saló, J. Baguña. Cell movement in intact and regenerating planarians. Quantitation using chromosomal, nuclear and cytoplasmic markers. *Development*, 89(1):57–70, 1985.
66. F. V. Santos. Studies on transplantation in Planaria. *Biol. Bullet.*, 57(3):188–197, 1929.
67. M. L. Scimone, S. W. Lapan, and P. W. Reddien. A forkhead transcription factor is wound-induced at the planarian midline and required for anterior pole regeneration. *PLoS Genet*, 10(1):e1003999, 2014.
68. J. Sherratt, P. Maini, W. Jäger, and W. Müller. A receptor based model for pattern formation in hydra. *Forma*, 10(2):77–95, 1995.
69. H. Shimizu, Y. Sawada, and T. Sugiyama. Minimum tissue size required for hydra regeneration. *Developmental biology*, 155(2):287–296, 1993.
70. S. Shostak. Inhibitory gradients of head and foot regeneration in Hydra viridis. *Developmental biology*, 28(4):620–635, 1972.
71. L. R. Smales and H. D. Blankespoor. The epidermis and sensory organs of Dugesia tigrina (Turbellaria: Tricladida). *Cell and Tissue Research*, 193(1):35–40, 1978.
72. T. Stückemann, J. P. Cleland, S. Werner, H. T.-K. Vu, R. Bayersdorf, S.-Y. Liu, B. Friedrich, F. Jülicher, and J. C. Rink. Antagonistic Self-Organizing Patterning Systems Control Maintenance and Regeneration of the Anteroposterior Axis in Planarians. *Developmental Cell*, 40(3):248–263, 2017.
73. M. Sureda-Gómez, J. M. Martín-Durán, and T. Adell. Localization of planarian β -CATENIN-1 reveals multiple roles during anterior-posterior regeneration and organogenesis. *Development*, 143(22):4149–4160, 2016.
74. J. Tasaki, N. Shibata, O. Nishimura, K. Itomi, Y. Tabata, F. Son, N. Suzuki, R. Araki, M. Abe, K. Agata, et al. ERK signaling controls blastema cell differentiation during planarian regeneration. *Development*, 138(12):2417–2427, 2011.
75. C. Tenbrock. Mathematical models for regeneration on the example of planarians. *PhD-Thesis, University of Münster (WWU), Germany*, 2017.
76. A. M. Turing. The chemical basis of morphogenesis. *Philosophical Transactions of the Royal Society B*, 1952.
77. A. M. Turing. Unpublished manuscripts and drafts. www.turingarchive.org

78. D. M. Umulis. Analysis of dynamic morphogen scale invariance. *Journal of The Royal Society Interface*, 6(41):1179–1191, 2009.
79. D. M. Umulis and H. G. Othmer. Mechanisms of scaling in pattern formation. *Development*, 140(24):4830–4843, 2013.
80. G. Webster. Studies on pattern regulation in hydra. *Development*, 16(1):123–141, 1966.
81. D. Wenemoser, S. W. Lapan, A. W. Wilkinson, G. W. Bell, and P. W. Reddien. A molecular wound response program associated with regeneration initiation in planarians. *Genes & Development*, 26(9):988–1002, 2012.
82. D. Wenemoser and P. W. Reddien. Planarian regeneration involves distinct stem cell responses to wounds and tissue absence. *Developmental biology*, 344(2):979–991, 2010.
83. S. Werner, T. Stückemann, M. Beirán Amigo, J. C. Rink, F. Jülicher, and B. M. Friedrich. Scaling and regeneration of self-organized patterns. *Phys. Rev. Lett.*, 114:138101, Apr 2015.
84. O. K. Wilby and G. Webster. Experimental studies on axial polarity in hydra. *Development*, 24(3):595–613, 1970.
85. J. N. Witchley, M. Mayer, D. E. Wagner, J. H. Owen, and P. W. Reddien. Muscle cells provide instructions for planarian regeneration. *Cell reports*, 4(4):633–641, 2013.
86. L. Wolpert. Positional information and the spatial pattern of cellular differentiation. *Journal of Theoretical Biology*, 25(1):1 – 47, 1969.
87. L. Wolpert. Positional Information and Pattern Formation in Development. *Developmental Genetics*, 1994.
88. O. Wurtzel, L. E. Cote, A. Poirier, R. Satija, A. Regev, and P. W. Reddien. A generic and cell-type-specific wound response precedes regeneration in planarians. *Developmental Cell*, 35(5):632–645, 2015.